Fabrication of Ni-Aluminides Long-Fiber Reinforced Ni Matrix Composite by a Reaction at Narrow Holes Method

Yoshimi Watanabe [1,a], Shingo Gonda [1], Hisashi Sato [1], Seiji Miura [2],

1 Graduate School of Engineering, Nagoya Institute of Technology, Gokiso-cho, Showa-ku, Nagoya 466-8555, Japan
2 Division of Materials Scinence and Engineering, Graduate School of Engineering, Hokkaido University, Kita-13, Nishi-8, Kita-ku, Sapporo 060-8628, Japan

Abstract

A novel method (reaction at narrow holes method, RANH method) to fabricate an intermetallic compound fiber / metal matrix composite is proposed. Narrow holes are drilled in the metal matrix *A*, and then metal fibers *B* are inserted into these holes. The assembly is heated to elevated temperatures to obtain molten metal *B* in the holes. Then the reaction between *A* and *B* should cause within the narrow holes. During the reaction, intermetallic compound of A_mB_n replaces the metal *B* keeping its fiber shape embedded in the metal matrix *A*. In this study, a Ni-aluminides fiber / Ni composite is fabricated by the novel method. Microstructure and mechanical property of these specimens were investigated. To evaluate the reaction during the RANH method, *in-situ* observation by laser scanning microscope and differential thermal analysis (DTA) were also carried out. From obtained results, effects of swaging treatment and heating condition on these microstructure and mechanical properties were discussed.

Keywords: Metal-matrix composites (MMCs), Fiber, Intermetallic compound, Reaction, Heating

a Corresponding author: Prof. Yoshimi Watanabe, Department of Physical Science and Engineering, Graduate School of Engineering, Nagoya Institute of Technology, Gokiso-cho, Showa-ku, Nagoya 466-8555, Japan, Tel.: +81-52-735-5624, e-mail: yoshimi@nitech.ac.jp

1. Introduction

Investigation and improvement of several mechanical properties such as yield stress, ultimate tensile stress, ductility and toughness are important concerns for the practical use of structural intermetallic compounds. To overcome the brittleness of monolithic intermetallic compounds at ambient temperature, the intermetallic compound reinforced metal based composites were fabricated by various researchers. For example, Al/Ni_3Al composite could be processed by powder metallurgy (Lieblich et al., 1997). Ni-aluminides-reinforced Ni-matrix composites could be fabricated by pulsed-current hot pressing (Mizuuchi et al., 2006). Reaction synthesis of NiAl/Ni micro-laminated composite from micro-foils of Ni and Al have been investigated by Kim et al., (2005). Platelet shaped Al_3Ti intermetallic compound particles dispersed Al based functionally graded materials were fabricated by centrifugal casting method (Watanabe et al., 2001a, Watanabe et al., 2017). Choi et al (2013) have fabricated an intermetallic compound reinforced Al alloy matrix composite using the reaction between porous Ni and molten Al.

Meanwhile, long-fiber composites with their promise of high specific strength, stiffness and creep resistance have been the subject of considerable research effort (Venkatesh and Dunand, 1999). The authors have proposed a reaction at narrow holes method (RANH method) as a fabrication method for an intermetallic compound long-fiber / metal matrix composite (Watanabe and Goto, 2003). Figure 1 schematically shows this fabrication process. Narrow holes having a small diameter are drilled in a metal matrix *A* as shown in Fig. 1(a). Metallic fibers *B* are inserted into these narrow holes as shown in Fig. 1(b). The assembly comprising the metal matrix *A* and metallic fibers *B* is heated to elevated temperatures to obtain molten metal B in the narrow holes. Then,

the reaction should occur in the narrow holes as shown in Fig. 1(c). After the processing, the assembly is cooled to ambient temperature. During the reaction, intermetallic compound of A_mB_n replaces the metal *B* keeping its fiber shape embedded in the metal matrix *A*. Consequently, the intermetallic compound A_mB_n fiber / metal matrix *A* composite can be fabricated as shown in Fig. 1(d).

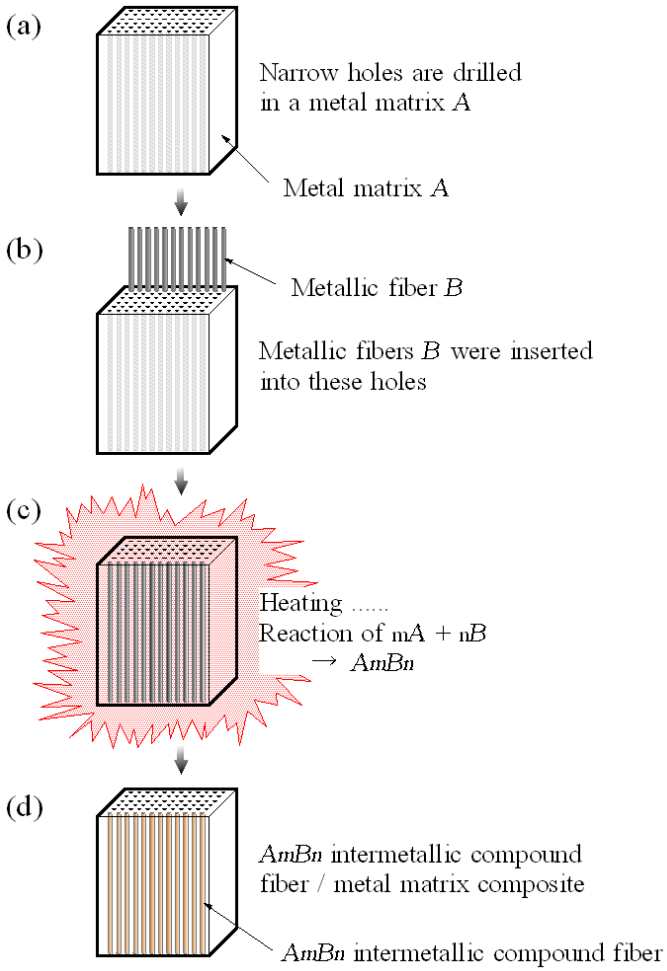

Fig. 1 Fabrication process of long fiber / metal matrix composite by RANH method.

In this study, Ni and Al are selected as the metal matrix and metallic fiber, respectively, since not a few intermetallic compounds appear in the Ni-Al system. The Ni-Al phase diagram, shown in Fig. 2, contains five intermetallic compounds ($NiAl_3$, Ni_2Al_3, NiAl, Ni_5Al_3 and Ni_3Al) (Massalski, 1996). Ni-aluminides are known to be ones

of the promising intermetallic compounds, since they have excellent mechanical and physical properties. For example, NiAl has the attractive combinations of low density (5.86 Mg/m^3), high melting point (1638 ^oC), high strength, good corrosion and oxidation resistance, and high thermal conductivity (Darolia, 1991). Ni_3Al is known to show the positive temperature dependence of strength (Suzuki et al., 1989). Recently, severe plastic deformation by high-pressure torsion of Ni_3Al is carried out by Ciuca et al. (2009). There exists a great deal of literature concerning the fabrication of Ni-aluminides. Janssen and Rieck (1967) studied reaction diffusion and Kirkendall-effect in Ni-Al system. Self-propagating high-temperature synthesis (SHS) of Ni_3Al from Ni and Al powders was studied by Lebrat et al. (1992). Amount of liquid phase during reaction synthesis of Ni aluminides was studied by Miura et al. (1997). Reaction synthesis processing of Ni–Al intermetallic compounds is reviewed by Morsi (2001). Such extensive studies on fabrication of Ni-aluminides result in enhancing our understanding of reaction between Ni and Al.

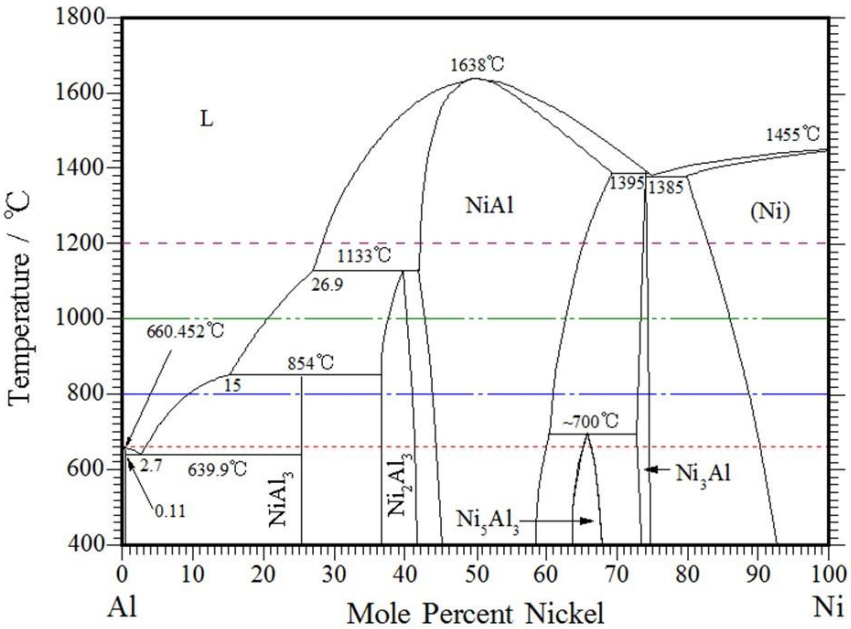

Fig. 2 Ni-Al phase diagram (Massalski, 1996).

In this study, the Ni-aluminides long-fiber / Ni matrix composites are fabricated by the RANH method under various process conditions. Microstructure and mechanical property of these specimens were investigated. From obtained results, effects of process condition on these microstructure and mechanical properties are discussed.

2. Experimental Procedure

2.1 RANH method

Matrix metal used in this study is Ni with a purity of 99%. A non-through narrow hole with ≧ 800 μm in diameter and 20 mm in depth was drilled in each pure Ni matrix cylindrical specimen with 18 mm in diameter and 30 mm in height. An Al fiber of 99.99% purity with ≦800 μm in diameter was inserted into the hole. The assemblies comprising the Ni matrix and Al fiber were heated at elevated temperatures for 30 min, 60 min and 120 min in air to obtain molten Al in the narrow hole. Molten metal equilibrates with $NiAl_3$, Ni_2Al_3 and NiAl phases at 800 °C, 1000 °C and 1200 °C, respectively. After the heating, the assembly was air-cooled to ambient temperature. The process conditions and notations of the specimens are listed in Table 1.

Table 1 Heating conditions.

Sample	Heating Temperature	Heating Time
1	660 °C	30 min
2	800 °C	30 min
3	1000 °C	30 min
4	1200 °C	30 min
5	1200 °C	60 min
6	1200 °C	120 min

2.2 Evaluation of Microstructure and Mechanical Property

All of the specimens were cut on the transverse section of the fiber at a position of 10 mm from the bottom of the narrow hole. Microstructures of the specimens were observed using a scanning electron microscope (SEM) by secondary electron imaging (SEI) on the transverse section of the fiber prepared by conventional grinding and polishing techniques. Energy dispersive X-ray (EDX) analysis was performed to investigate chemical composition of specimens. For evaluating mechanical property, micro Vickers-hardness (HV) indentation tests were carried out for all specimens at room temperature (RT). The load and the loading time were 100g and 30 s, respectively.

2.3 In-situ Observation of Reaction by Laser Scanning Microscope and DTA

To understand the reaction during the RANH method, *in-situ* observation by laser scanning microscope and differential thermal analysis (DTA) were carried out. The top surface of the cylindrical specimen was carefully polished for observing the reaction at Ni-Al interface during heating in a gold image furnace under Ar flow atmosphere using a Laser Scanning Confocal Microscope (type 1LM21H, Lasertech Ltd., Japan). The specimen was heated two times up to 1273 ^{o}C with a heating rate of about 300 ^{o}C /min and kept for 10 min at the maximum temperature, then cooled.

DTA was carried out using a cylindrical specimen with an Al fiber, where dimensions of the specimen are about 3 mm in diameter and 3 mm in height. This specimen was set in an Al_2O_3 crucible, then placed in an furnace for differential thermal analysis (RIGAKU Thermal Analysis System TAS 300, model 8110D). Under an Ar

atmosphere, the specimen temperature was heated up from RT to 1200 °C two times with a heating rate of 10 °C /min and kept for 10 min at the maximum temperature.

2.4 Swaged Samples

To study the effect of fiber diameter on the microstructure, the assembly comprising the Ni matrix and Al fiber was rotary-swaged at room temperature. Rotary swaging is a cold bulk forming process. The diameter of the workpiece is reduced incrementally by oscillating movement of the tools. (Herrmann et al., 2016). Al fiber with 1mm diameter and 20mm length were inserted into the hole located at the center of Ni cylinder whose diameter was 18 mm. Table 2 shows the conditions of swaging treatment. The swaged samples are, then, heated at 660 °C for 30 min, which is the same for specimen 1.

Table 2 Swaging conditions.

Sample	Swaging Ratio	Initial Fiber Diameter	Heating Temperature and Time
7	5.6 %	944μm	660 °C , 30 min
8	16.7 %	833μm	660 °C , 30 min
9	27.8 %	722μm	660 °C , 30 min
10	38.9 %	611μm	660 °C , 30 min

3. Results and Discussion

3.1 DTA analysis

DTA profile is shown in Fig. 3. During the heating in the 1st run of the analysis (Fig. 3 (a)), there is an endothermic reaction at around 660 °C, which corresponds to the melting of Al fiber. According to the Ni-Al binary phase diagram, the peaks at around 850 °C and 1130 °C are the melting of $NiAl_3$ and Ni_2Al_3, respectively. As no peaks corresponding to the solidification of $NiAl_3$ and Ni_2Al_3 during the cooling in the 1st run,

the large peak at around 800 °C during cooling is presumably due to the supercooling of the solidification of $NiAl_3$. On the other hand, no reaction corresponding to the melting point of Al is found during the cooling of 1st run and heating in the 2nd run. Instead, several peaks were recognized at around 630 °C, 850 °C and 1130 °C, corresponding to the eutectic reaction (Al+ $NiAl_3$ ◁-▷ liquid), the melting of $NiAl_3$ and Ni_2Al_3, respectively, during the heating in the 2nd run. Comparing to the result of 1st run, the peak heights become larger because the amount of the intermetallic phases increased. However, during the cooling in the 2nd run (Fig. 3 (b)), no exothermic reactions were recognized, presumably due to the consumption of Al-rich molten metal during the formation of NiAl and/or Ni_3Al by diffusion of constituent elements. Small peaks at around 370 °C are the curie temperature of Ni.

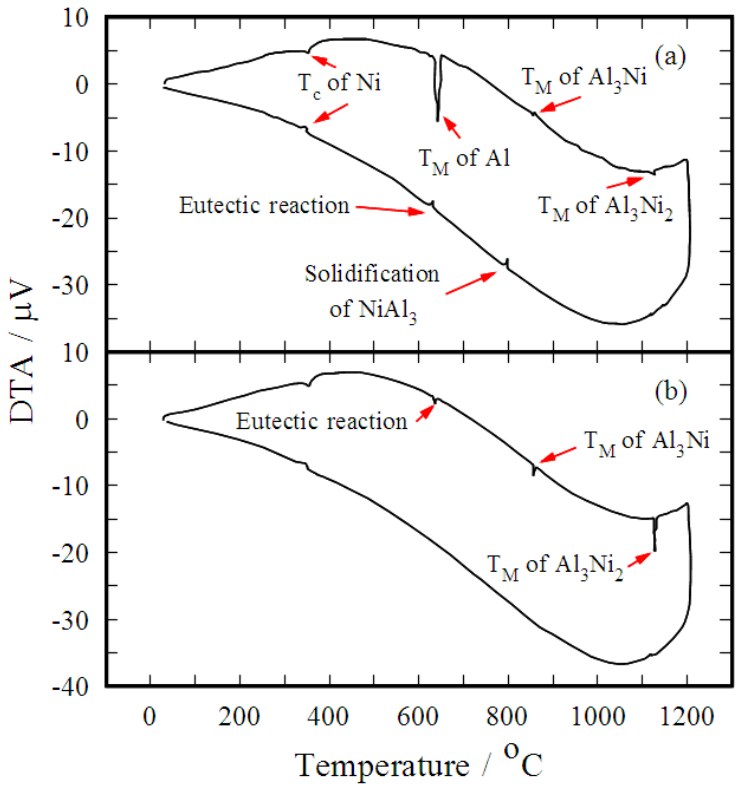

Fig. 3 The heat pattern and DTA profile.

3.2 Microstructure

Figure 4 shows the result of *in-situ* observation by laser scanning microscope. During heating, the Al fiber at the center of the specimen was melted at around its melting temperature as shown in Fig. 4, then the surface colors of Ni near molten Al fiber changed immediately, presumably due to the liquid-solid reaction between molten Al and surrounding solid Ni. Although the interface between solid Ni and molten Al was unclear because the surface was covered by alumina layer, extension of molten area can be observed. During the cooling, thermal arrest appears at about 600 ^{o}C, indicates an invariant reaction of eutectic reaction occurs.

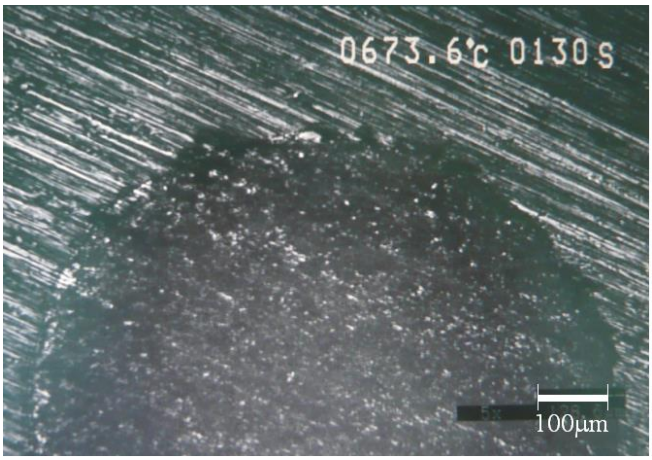

Fig. 4 Result of in-situ observation by laser scanning microscope. The Al fiber at the center of the specimen was melted at around its melting temperature.

Figure 5 shows the cross section view of the specimen 1 processed at 660 ^{o}C for 30 min observed with SEM SEI. Lower magnification photograph, higher magnification photographs at fiber center region and the fiber / matrix interface region are shown in Figs. 5 (a), (b) and (c), respectively. In Fig. 5 (a), initial diameter of the Al fiber (800μm) is indicated by the upper scale bar at the top of the figure. The Al fiber was alloyed with Ni, and the obtained fiber shows a microstructure consisting of the light gray network

surrounding the darker gray phase (Fig. 5 (b)). According to composition analysis by EDX, the light gray network and the darker gray phase are identified to be ($NiAl_3$ + Al) eutectic structure and α-Al, respectively. The $NiAl_3$ intermetallic compound is widely accepted to be the first equilibrium phase to grow at Al/Ni interface, and in many cases no intermediate phases were observed prior to the formation of $NiAl_3$ phase. Colgan et al., (1985) reported that initial phase of $NiAl_3$ forms in thin-film Al/Ni, Al/NiAl/Ni and Al/Ni_3A1 diffusion couples. The first intermetallic phase of $NiAl_3$ forms by heterogeneous nucleation during reactions in multilayer Al/Ni films (Ma et al., 1991).

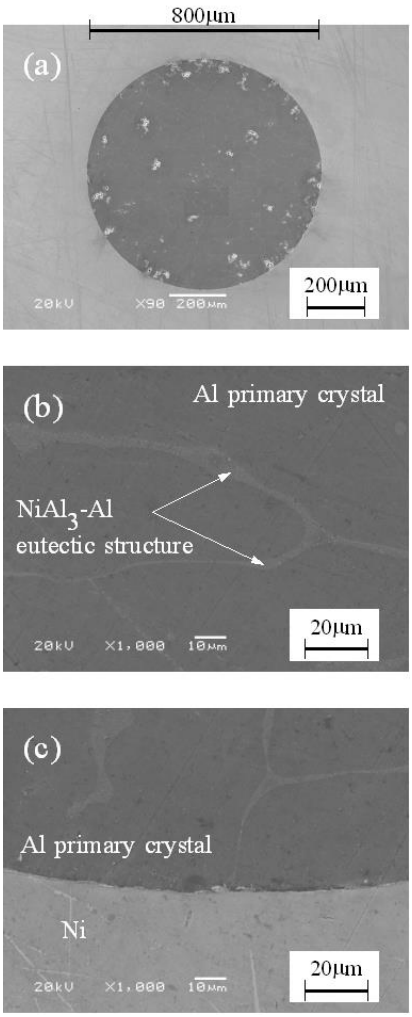

Fig. 5 Cross section view of the specimen 1. Lower magnification photographs are shown in (a), whereas higher magnification photographs at fiber center region and the fiber / matrix interface region are shown in (b) and (c), respectively.

The solidification reaction within the fiber can be described as,

$$L \rightarrow L + Al \text{ (primary phase)}$$
$$L \rightarrow NiAl_3 + Al \quad \text{(eutectic reaction at 639.9}^{o}\text{C)} \quad (1).$$

Then the final microstructure of Al primary phase and ($NiAl_3$ + Al) eutectic structure are formed. This indicates that the chemical composition of the molten fiber was hypoeutectic having a composition between 0.11mol% Ni and 2.7 mol% Ni. Although dissolution of Ni in liquid Al is observed, the obtained fiber keeps its original shape, as shown in Fig. 5 (a). Moreover, no intermediate phase is observed around the fiber / matrix interface (Fig. 5 (c)). This suggests migration of Al atoms from liquid Al into the solid Ni was very limited.

Cross section view of the fabricated fiber within the specimen 2 processed at 800 ^{o}C for 30 min is shown in Fig. 6 (a). The average diameter of the fiber becomes 894 μm. Fiber center and the fiber / matrix interface regions are shown in Figs. 6 (b) and (c), respectively. Relatively large pores are observed at around the fiber / matrix interface region. It is seen from Fig. 6 (b), core region of the fiber shows composed of primary $NiAl_3$ phase and ($NiAl_3$ + Al) eutectic structure. Although the mean chemical composition of the core region changes from place to place, its range is from 4.5 mol% Ni to 7.9 mol% Ni. Therefore, the chemical composition of the molten fiber was hypereutectic having a composition between 2.7 mol% Ni and about 9 mol % Ni at which

Al-rich molten metal equilibrates with $NiAl_3$ at 800 ^oC. Solidification process of molten fiber can be expressed as,

$$L \rightarrow L + NiAl_3 \text{ (primary phase)}$$
$$L \rightarrow NiAl_3 + Al \text{ (eutectic reaction at } 639.9^oC) \quad (2).$$

Consequently, the final microstructure containing primary $NiAl_3$ phase plus ($NiAl_3$ + Al) eutectic structure is formed. Moreover, an interfacial phase appeared between the Ni matrix and the fiber core region. The result of EDX indicates that the layer is Ni_2Al_3 intermetallic compound. Inner side of this Ni_2Al_3 intermetallic compound layer, $NiAl_3$ intermetallic compound is also observed, which is in agreement with the literature (Tsao and Chen, 1995). Formation mechanism of this Ni_2Al_3 interlayer will be discussed later.

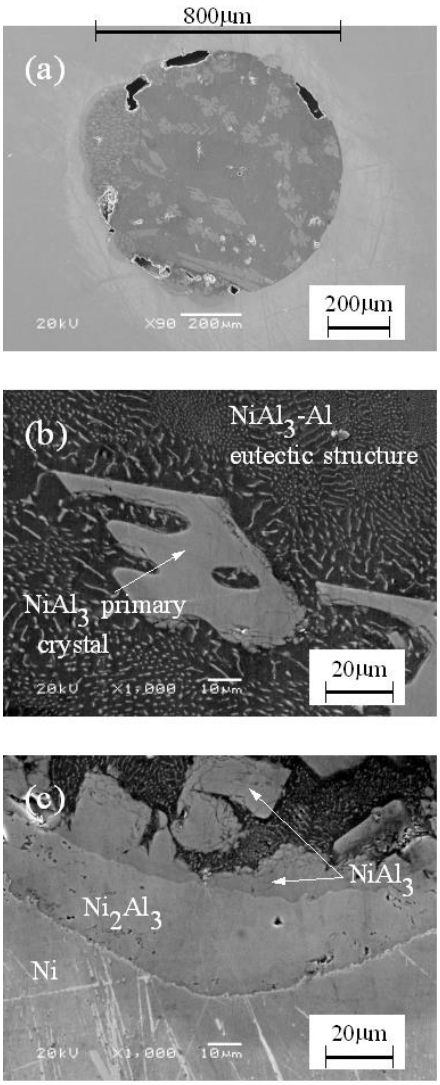

Fig. 6 Cross section view of the specimen 2. Lower magnification photographs are shown in (a), whereas higher magnification photographs at fiber center region and the fiber / matrix interface region are shown in (b) and (c), respectively.

Figures 7 (a), (b) and (c) show lower magnification photograph, higher magnification photographs at fiber center region and the fiber / matrix interface region, respectively, of the specimen 3 processed at 1000 °C for 30 min. The final microstructure is grains composed of un-reacted Ni_2Al_3 core with outer $NiAl_3$ plus ($NiAl_3$ + Al) eutectic structure. During solidification of molten fiber, the primary Ni_2Al_3 phase forms at the

liquidus temperature of the alloy. This is followed by the formation of $NiAl_3$ phase at 854ºC in the manner of the peritectic reaction. At the eutectic temperature of 639.9ºC, eutectic $NiAl_3$ + Al structure appears. The un-reacted Ni_2Al_3 presents at the core of $NiAl_3$ phase. The microstructure of core region of fiber was formed though the following stages.

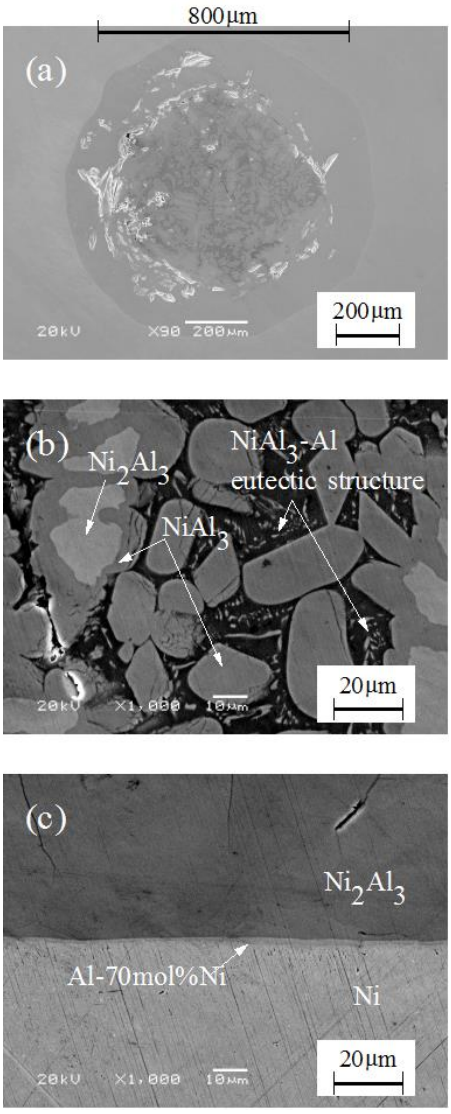

Fig. 7 Cross section view of the specimen 3. Lower magnification photographs are shown in (a), whereas higher magnification photographs at fiber center region and the fiber / matrix interface region are shown in (b) and (c), respectively.

$L \rightarrow L + Ni_2Al_3$ (primary phase)

$L + Ni_2Al_3 \rightarrow NiAl_3$ (peritectic reaction at 854°C,
there may be some un-reacted Ni_2Al_3)

$L + NiAl_3 \rightarrow NiAl_3 + Al$ (eutectic reaction at 639.9°C) (3).

Judging from the obtained microstructures, the chemical composition of the molten fiber is higher than 15 mol% Ni because Ni_2Al_3 is the primary phase, and is lower than about 20 mol% Ni at which Al-rich molten metal equilibrates with Ni_2Al_3 at 1000 °C. Surrounding the fiber core region, interlayer of Ni_2Al_3 intermetallic compound was observed. Moreover, very thin interlayer was also formed between Ni_2Al_3 interlayer and Ni matrix, and its concentration of Ni was around 70 mol%. The average diameter of the fiber including the interlayers was 973 μm.

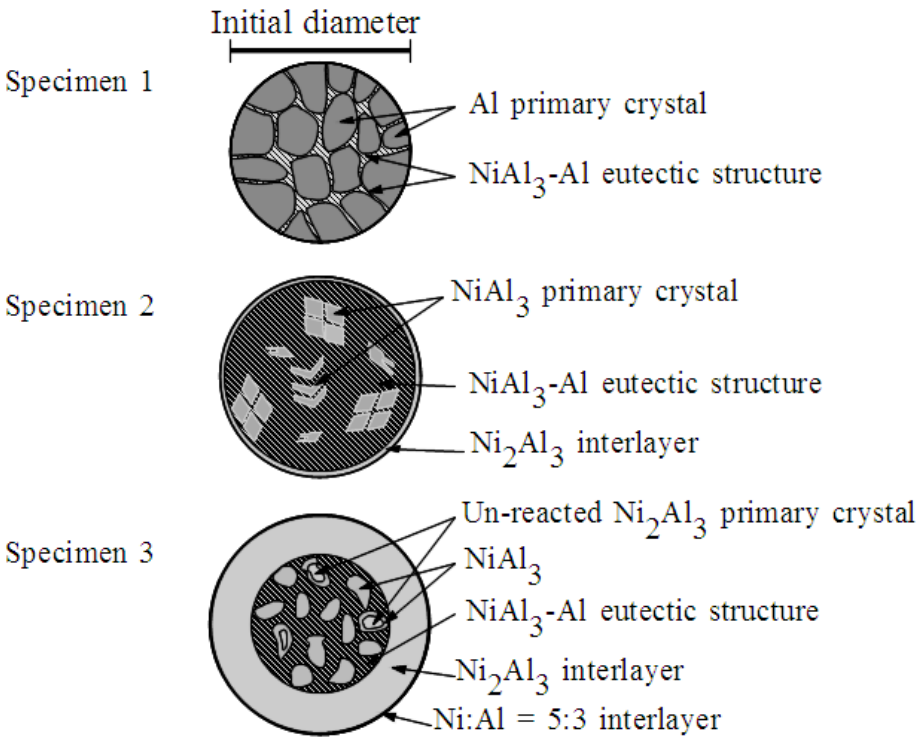

Fig. 8 Schematic illustrations showing the final microstructure of specimens 1 to 3.

Figure 8 summarizes the final microstructures of specimens 1 to 3. In the cases of processing at 660 ºC and 800 ºC (specimens 1 and 2), the chemical composition of molten Al fiber becomes hypoeutectic and hypereutectic, respectively. On the other hand, in case of high processing temperature (specimen 3), the chemical composition of molten Al fiber becomes from 15 mol% Ni to 20 mol% Ni.

The experimental results of specimens 2 and 3 processed at 800 and 1000 ºC allowed us to consider the core region (molten alloy) at process temperatures becomes equilibrium state which can be explained by the Al-Ni phase diagram. Therefore, expected microstructural evolution of specimens 4 to 6 processed at 1200 ºC can be illustrated as shown in Fig. 9. Initial microstructure is shown in Fig. 9 (a). At 1200 ºC, Ni atoms diffuse into molten Al, and Al atoms diffuse into Ni matrix, as shown in Fig. 9 (b). As a result, molten alloy core region has a chemical composition of about 28 mol%Ni, which is surrounded by NiAl intermetallic compound layer with chemical composition of about 42 mol% Ni. Outer of the NiAl intermetallic compound layer, Ni_3Al intermetallic compound must be formed in equilibrium state. From consideration of mass balance of Al atoms, the shrinkage of core region must be appeared by the time evolution, as shown in Fig. 9 (c). This is because the chemical composition of core region keeps constant chemical composition (equilibrium state at 1200 ºC and that is Al-28 mol%Ni). At the same time, expansion of interlayer must be appeared because of diffusion of Al atoms into Ni matrix and formation of intermetallic compound phases. During the cooling from 1200 ºC to 1133 ºC, primary crystal of NiAl intermetallic compound phase crystallized from molten Al-Ni alloy, as shown in Fig. 9 (d). At 1133 ºC, Ni_2Al_3 phase formed by the peritectic reaction from Al-rich NiAl primary phase. On the other hand, $NiAl_3$ phase formed by the peritectic reaction at 854ºC. Since the cooling rate is relatively higher, un-reacted NiAl and Ni_2Al_3 phases remain (similar to specimen 3), results in an Al rich

molten metal, and then the eutectic phases at fiber core region are formed. The second reaction around the interface region is shown in Fig. 9 (e). Solidification process of molten fiber can be, then, expressed as

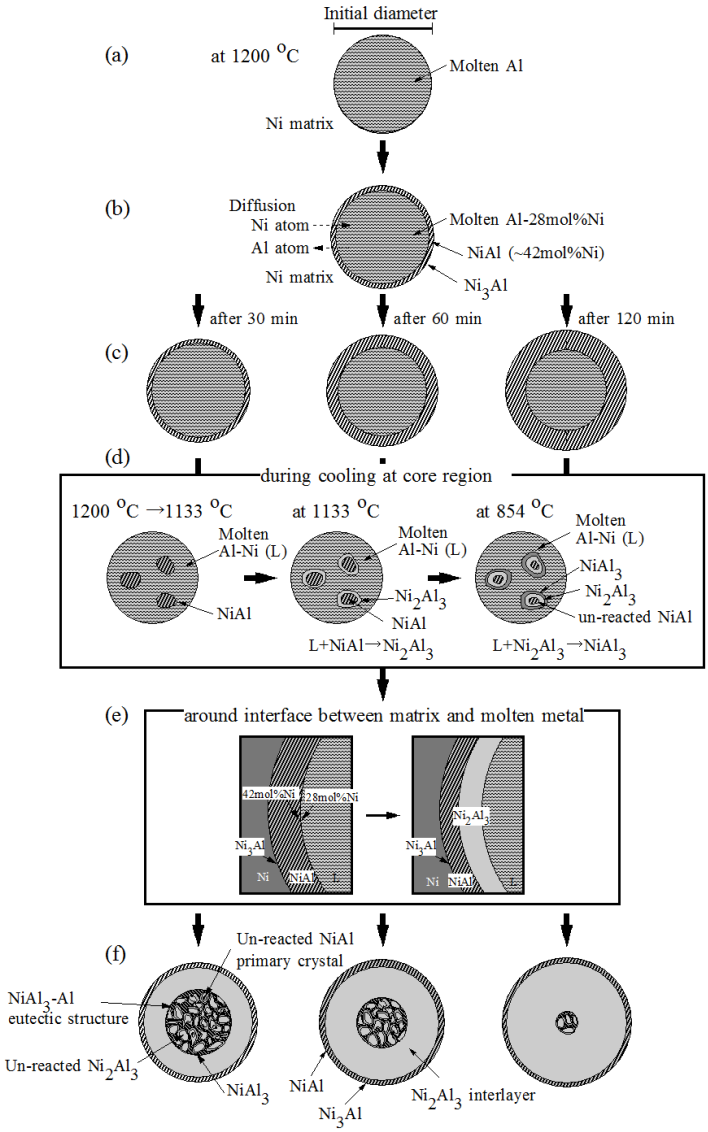

Fig. 9 Expected microstructural evolution of specimens 4 to 6 processed at 1200 °C. Initial state and microstructural evolution at 1200 °C are shown in (a) and (b), respectively. Shrinkage of core region and expansion of interlayer must be appeared by the time evolution, as shown in (c). Microstructural evolution during the cooling from 1200 °C to 854 °C is shown in (d). (e) and (f) show the reaction around the interface region and final microstructures of specimens 4 to 6, respectively.

$L \rightarrow L + NiAl$ (primary phase)

$L(28\ mol\%Ni) + NiAl(42\ mol\%Ni) \rightarrow Ni_2Al_3$ (peritectic reaction at 1133°C)

$L + Ni_2Al_3 \rightarrow NiAl_3$ (peritectic reaction at 854°C)

$L \rightarrow NiAl_3 + Al$ (eutectic reaction at 639.9°C) (4).

Final microstructures of specimens 4 to 6 are shown in Fig. 9 (f).

The results from specimen 4 processed at 1200 °C for 30 min are shown in Fig. 10. Large shrinkage cavity is presented in the core region of the fiber as shown in Fig. 10 (a). Fig. 10 (b) shows the interlayer structure which consists of two layers, namely thicker interlayer of Ni_2Al_3 intermetallic compound encircled by a rim of Al-65 mol%Ni, and embedded into a matrix of Ni. The total fiber diameter now becomes 1036 μm.

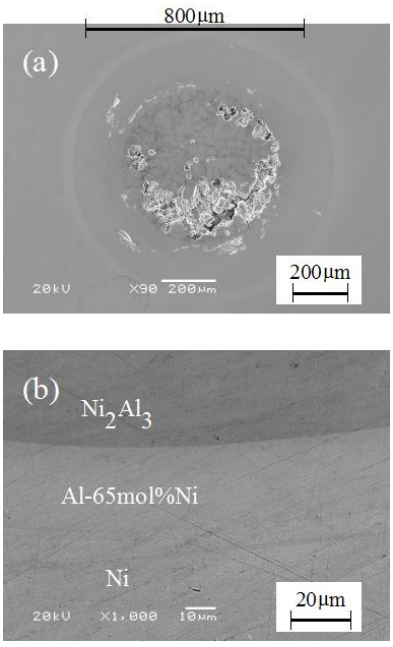

Fig. 10 Cross section view of the specimen 4. Lower magnification photograph is shown in (a), whereas higher magnification photograph at the fiber / matrix interface region are shown in (b).

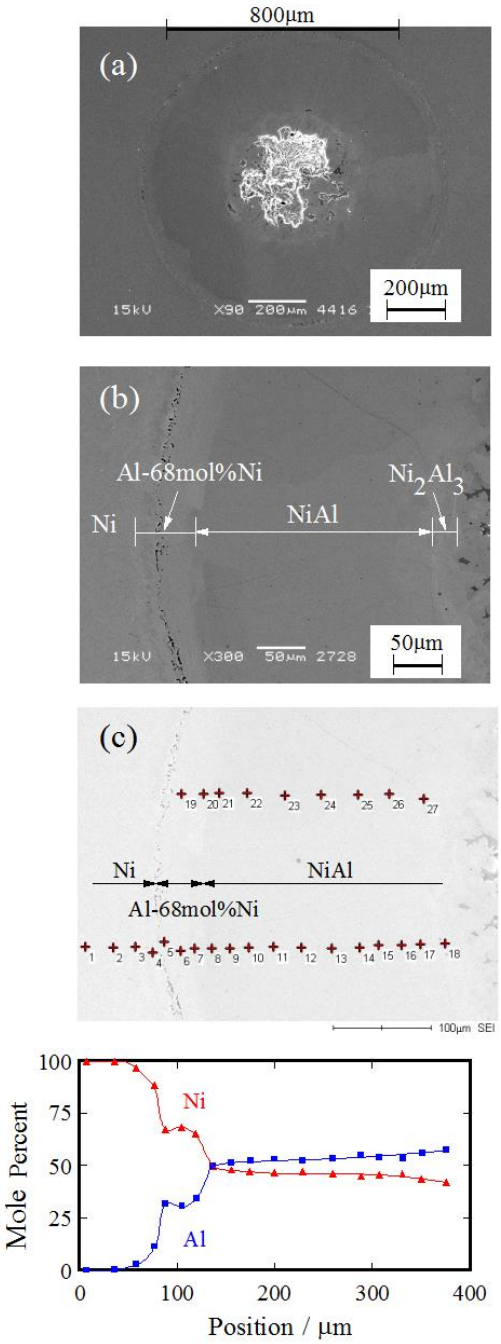

Fig. 11 Cross section view of the specimen 5. Lower magnification photograph and higher magnification photograph at the fiber / matrix interface region are shown in (a) and (b), respectively. Concentration profiles of Al and Ni across the interlayer region are shown in (c).

Figures 11 (a) and (b) show the microstructures of the specimen 5 processed at 1200 ^{o}C for 60 min. Core region of the fiber consists of $NiAl_3$ formed in the manner of peritectic reaction, un-reacted Ni_2Al_3 and ($NiAl_3$ + Al) eutectic structure, which is consistent with the results from specimen 4. However, the area of fiber core region in specimen 5 is smaller, as expected. Concentration profiles of Al and Ni across the interlayer region are shown in Fig. 11 (c). As can be seen, three different interlayers were observed: outer layer has low Al and high Ni concentrations, interior layer has the same level of Al and Ni concentrations and therefore indentified as NiAl intermetallic compound phase, and inner layer has a stoichiometric chemical composition of Ni_2Al_3. It must be noted here, interior layer of NiAl has a chemical compositional gradient and higher Ni content is found for outer region, since NiAl intermetallic compound is not a line compound as shown in Fig. 2. Large pores were observed at around the center region. Also cracks can be found at Al- 68 mol%Ni microstructure / Ni interface. The total fiber diameter is 1050 μm.

Specimen 6, processed at 1200 ^{o}C for 120 min, exhibits the similar microstructure as specimen 5 processed at 1200 ^{o}C for 60 min, but the amount of appeared phases and microstructure is different, as shown in Fig. 12. The thickness of interlayers becomes larger, while the area of fiber core region becomes smaller. Large pore was not found around the core region, while obvious cracks can be observed at Al- 68 mol%Ni microstructure / Ni interface, as shown in Fig. 12 (a). The total fiber diameter is 1058 μm. Figure 12 (b) shows the evidence of the formation of Ni_2Al_3 and $NiAl_3$ phases by the successive peritectic reactions at 1133^{o}C and 854^{o}C, respectively. Un-reacted NiAl and Ni_2Al_3 phases remain, results in an Al rich molten metal, and therefore the eutectic reaction occurred at fiber core region. As can be seen from Fig. 12 (c), the interlayer structure consists of three layers, namely Ni_3Al, NiAl and Ni_2Al_3 intermetallic compound

layers. From Fig. 12 (d), the chemical compositional gradient can also observed within the NiAl layer.

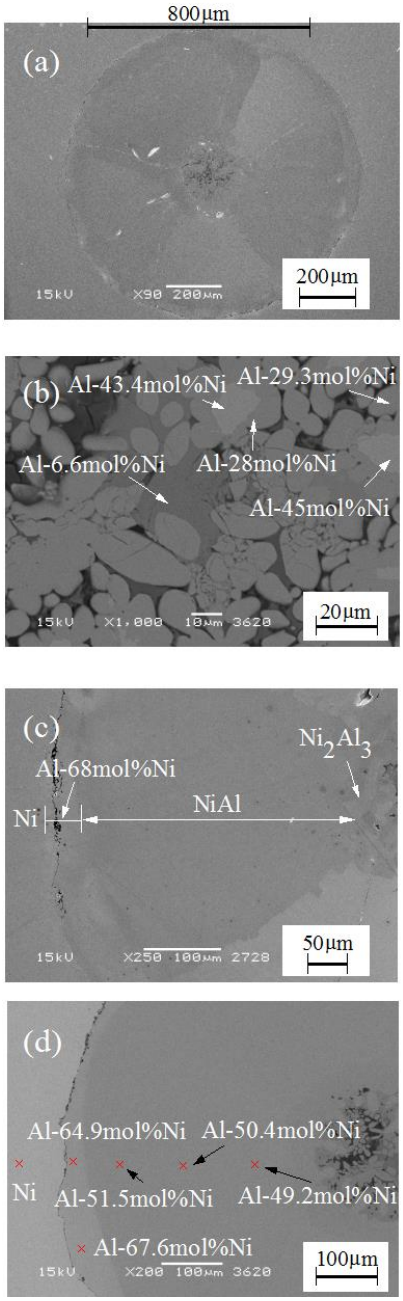

Fig. 12 Cross section view of the specimen 6. Lower magnification photographs are shown in (a), whereas higher magnification photographs at fiber center region and the fiber / matrix interface region are shown in (b) and (c), respectively. Results of EDX analysis is shown in (d).

Now, we will discuss the formation mechanism of observed interlayers. Supposing the diameters of the initial Al fiber and core region after reaction are d_0 and d_1, respectively, and outer radius of interlayer is d_2, as shown in Fig. 13. The number of Al atoms within the unit length of fiber before the reaction, those of the liquid region and interlayer region after reaction are $n_0 \times \pi(d_0/2)^2/V_{Al}$, $n_1 \times \pi(d_1/2)^2/V_1$ and $n_2 \times \pi((d_2/2)^2-(d_1/2)^2)/V_2$, respectively, where V_{Al}, V_1 and V_2 are atomic volumes of liquid pure Al, liquid Al-Ni alloy and intermetallic phase, respectively, and n_0, n_1 and n_2 are atomic fraction of Al at fiber region before and after the reaction and interlayer region, respectively. From the mass balance of Al atoms, relation between d_1 and d_2 can be, therefore, expressed as,

$$n_0 \times \pi(d_0/2)^2/V_{Al} = n_1 \times \pi(d_1/2)^2/V_1 + n_2 \times \pi((d_2/2)^2-(d_1/2)^2)/V_2 \quad (5).$$

where $n_0 = 1$. Therefore,

$$d_1 = \sqrt{\left(\frac{d_0^2/V_{Al} - n_2 d_2^2/V_2}{n_1/V_1 - n_2/V_2}\right)} \quad (6)$$

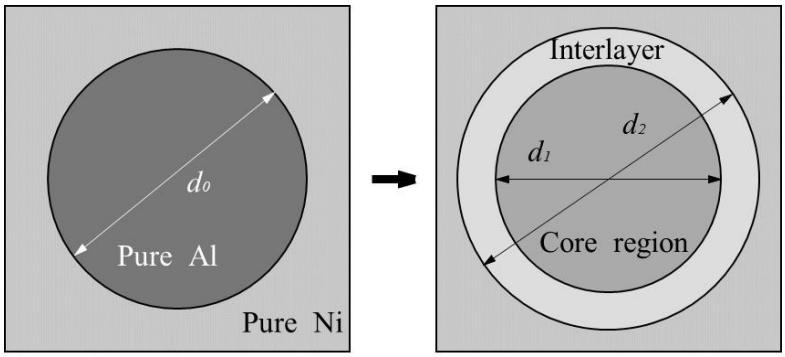

Fig. 13 Schematic illustrations of fiber before and after the reaction.

Meanwhile, the composition dependence of average atomic volume in Al-Ni binary system is shown in Fig. 14 (Miura et al., 2005). It must be noted here that the average atomic volume decreases linearly with increasing the atomic percent Ni when atomic percent Ni is less than 40 %. It is known that the density of Al at 25ºC is 2.70 Mg/m^3. Leitner et al. (2017) present experimentally obtained thermophysical properties of liquid Al. According to their study, density of molten Al at temperature range of $660 \leq T \leq 1407$ (ºC) can be given by

$$\rho\,(\mathrm{L}) = 2670 - 0.299 \times (T + 273) \qquad (7).$$

The density of molten Al at 1200 ºC is, therefore, estimated to be 2.230 Mg/m^3. Using these values, average atomic volumes of molten pure Al and Al-Ni alloy at elevated temperature can be roughly estimated, and 20.1 x 10^{-3} nm^3 for pure Al, 18.2 x 10^{-3} nm^3 for Al-28 mol%Ni and 18.7 x 10^{-3} nm^3 for Al-20 mol%Ni at 1200 ºC. Moreover, coefficient of thermal expansion (CTE) for NiAl intermetallic compound at various temperatures was studied by Honma et al. (1998), and *i.e.*, 15.4 x 10^{-6} / ºC at 327 ºC and 15.6 x 10^{-6} / ºC at 727 ºC, for example. The atomic volume of NiAl at elevated temperature can be calculated by density and coefficient of thermal expansion using eqn. (8),

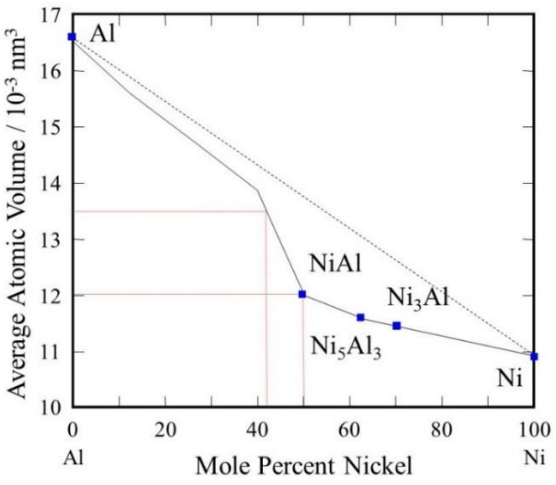

Fig. 14 Composition dependence of average atomic volume in Al-Ni binary system after Miura et al. (2005).

$$V_T = V_{RT}(1+\alpha\Delta T)^3 \qquad (8)$$

where V_T, α, ΔT and V_{RT} are atomic volume at temperature T, CTE, temperature change and atomic volume at room temperature, respectively. The atomic volume of NiAl with stoichiometric composition at 1200 ºC is, then, determined to be about 12.7x 10^{-3} nm^3 using eq. (8), while 14.3x 10^{-3} nm^3 for NiAl with 42 mol% Ni, if α is fixed to be 15.6 x 10^{-6} / ºC.

Let us consider the relation between d_1 and d_2 at 1200 ºC. Since molten alloy at core region has a chemical composition of about 28 mol%Ni, which is surrounded by NiAl intermetallic compound layer with chemical composition of about 42 mol% Ni at equilibrium state, the following values, $n_0 = 1$, $n_1 = 0.72$, $n_2 = 0.58$, $V_{Al} = 20.1 \times 10^{-3}$ nm^3, $V_1 = 18.2 \times 10^{-3}$ nm^3, $V_2 = 14.3\times 10^{-3}$ nm^3, $d_0 = 800 \times 10^3$ nm, are used for calculation. The results are shown in Fig. 15. It is seen from this figure that d_2 becomes smaller when

d_1 becomes smaller. This result conflicts with experimental results, namely the extension of interlayer region during reaction cannot be explained. As shown in Fig. 12 (d), the chemical compositional gradient from 49.2 mol%Ni to 51.5 mol%Ni was observed within the NiAl layer. Therefore, next calculation was carried out for $n_0 = 1$, $n_1 = 0.72$ (Al-28 mol%Ni) and $n_2 = 0.5$ (Al-50 mol%Ni), where $V_2 = 12.7 \times 10^{-3}$ nm^3, and results are also shown in Fig. 15. In this case, d_2 value becomes larger when d_1 value becomes smaller, but the extension of interlayer region during reaction is very small. This is because the atomic volume of NiAl with chemical compound of 50 mol%Ni is much smaller than that of 42 mol%Ni as shown in Fig. 14. Another calculation is done for $n_0 = 1$, $n_1 = 0.80$, $n_2 = 0.5$ ($V_{Al} = 20.1 \times 10^{-3}$ nm^3, $V_1 = 18.7 \times 10^{-3}$ nm^3, $V_2 = 12.7 \times 10^{-3}$ nm^3, $d_0 = 800 \times 10^3$ nm), and results are also shown in Fig. 15. As can be seen, d_2 becomes larger when d_1 becomes smaller. Although the data is not presented here, it was found that the extension of molten area at elevated temperature was observed by an *in-situ* observation using laser scanning microscope. Therefore, calculated result is in qualitatively agreement with the results obtained by SEM shown in Figs. 10 to 12, and laser scanning microscope.

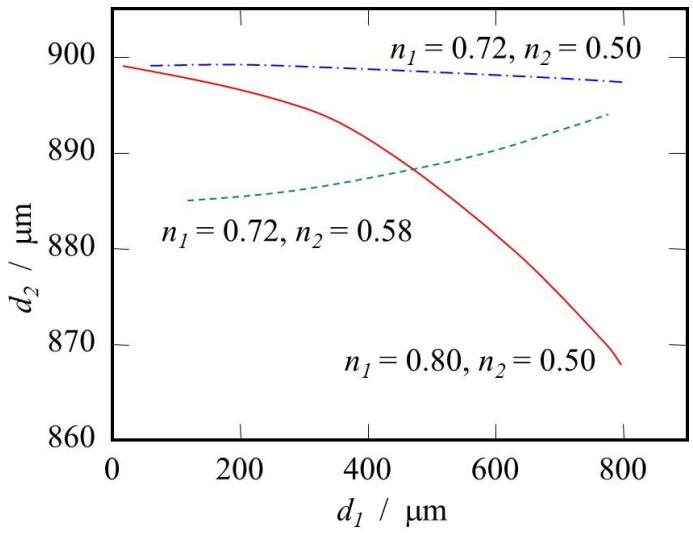

Fig. 15 Relation between d_1 and d_2 at 1200 °C. Calculation was carried out for n_1 = 0.72 and n_2 = 0.58, n_1 = 0.72 and n_2 = 0.50, and n_1 = 0.80 and n_2 = 0.50.

Now, we would like to plot the experimental data on Fig. 15, and the results are shown in Fig. 16. It is seen from this figure that the d_1 vs d_2 curve obtained by experimentally shows a similar trend as that obtained by calculation for n_0 = 1, n_1 = 0.80, n_2 = 0.5, namely d_2 becomes larger when d_1 becomes smaller. Therefore, atomic fraction of Al at fiber region after the reaction and interlayer region must be 0.80 and 0.5, respectively. However, d_2 value is much larger than that expected. This is because that, during the process, the molten Al alloy could be provided from upper part of assembly, and mass balance had been broken down. Again, we would like to discuss the average atomic volume in Al-Ni binary system shown in Fig. 14. The average atomic volumes of intermetallic compounds are much smaller than that estimated by liner relationship betw een Al and Ni. This indicates that the density of Al-Ni increases and large shrinkage defects, such as voids, develop when the intermetallic compounds formed. However, since not a lot of voids were observed at fiber region, molten Al exists at upper acts as riser, which is reservoir for excess molten metal to feed the casting as it shrinks during solidification. Then equation (5) can be rewritten as following;

$$n_0 \times \pi(d_0/2)^2/V_{Al} \times \beta = n_1 \times \pi(d_1/2)^2/V_1 + n_2 \times \pi((d_2/2)^2 - (d_1/2)^2)/V_2 \qquad (9).$$

where β is mass balance factor. Therefore, when n_0 = 1,

$$d_1 = \sqrt{\left(\frac{\beta d_0^2/V_{Al} - n_2 d_2^2/V_2}{n_1/V_1 - n_2/V_2}\right)} \qquad (10)$$

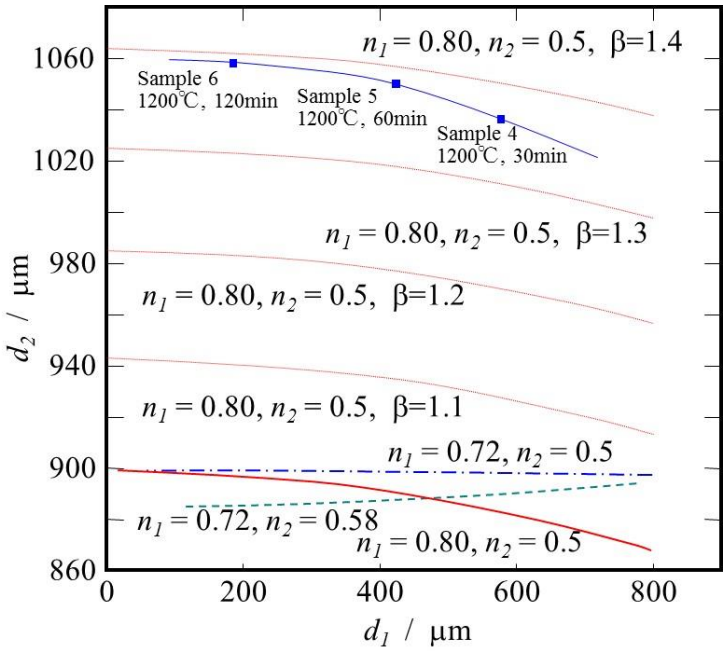

Fig. 16 Experimentally obtained relation between d_1 and d_2.

The relation between d_1 and d_2 calculated with β =1.1, 1.2, 1.3 and 1.4 for n_1 = 0.80, n_2 = 0.50 at 1200 °C are also shown in Fig. 16. As can be seen from this figure, experimental data lies between β =1.3 and 1.4. Moreover, the stronger effects of riser is found for longer keeping time at 1200 °C.

3.4 Swaged Samples

If the above discussion is correct, not only the processing temperature but also the diameter of fiber may also influence the microstructure of the fiber. To study the effect of fiber diameter on the microstructure, the assembly comprising the Ni matrix and Al fiber was rotary-swaged at room temperature.

Figures 17 (a), (b), (c) and (d) show the microstructures of swaged specimens 7, 8, 9 and 10, respectively. Initial diameters of the Al fiber are indicated by the upper scale bars. One may have noticed that the core region of the fiber becomes smaller, while the

interlayer maintains same thickness when the swaging ration becomes larger. Dimensions of fibers in specimens 7 to 10 are summarized in Table 3. It is also seen that these microstructures are different from the microstructure of specimen1 (shown in Fig. 5), although the processing temperature is the same. Microstructure of the core region of the fibers consists primary $NiAl_3$ phase and ($NiAl_3$ + Al) eutectic structure, as shown in Fig. 18 (a). This core region is surrounded by interlayers consisted with $NiAl_3$ and Ni_2Al_3 intermetallic compounds, as shown in Fig. 18 (b).

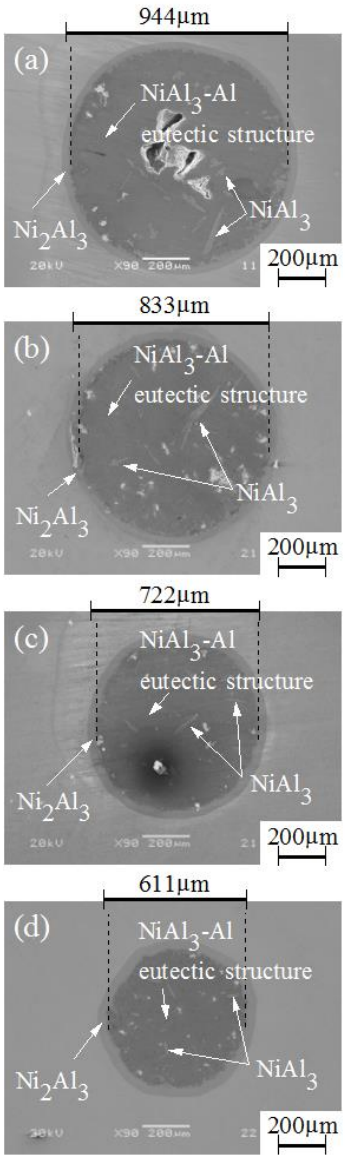

Figs. 17 (a), (b), (c) and (d) Cross section views of the specimens 7, 8, 9 and 10.

Table 3 Dimensions of fibers in swaged specimens.

Sample	Initial Fiber Diameter	Core Diameter	Layer Thickness	Total Diameter
7	944μm	879μm	37μm	953μm
8	833μm	784μm	39μm	862μm
9	722μm	678μm	44μm	766μm
10	611μm	559μm	47μm	653μm

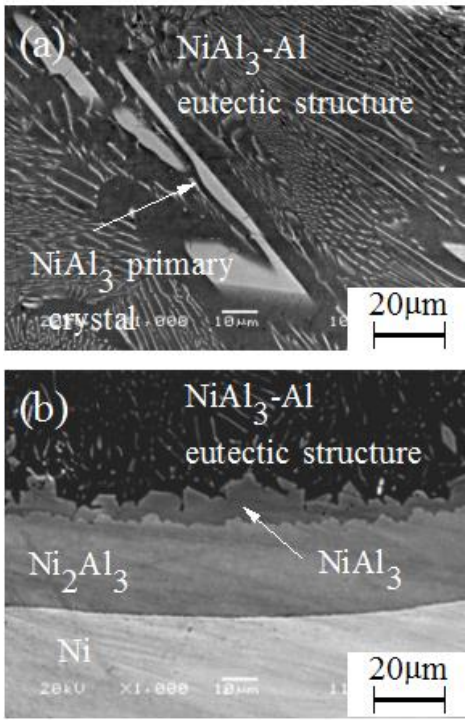

Fig. 18 SEM SEI images showing core region (a) and fiber / Ni matrix interface (b) in Specimen 7.

Again, we will discuss the formation of interlayer of the swaged specimens. Since the density of molten Al at 660 ºC is 2.391 Mg/m^3 (Leitner et al. 2017), V_{Al} and V_1 for Al-2 mol%Ni at 660 ºC are 18.75 x 10^{-3} nm^3 and 18.65 x 10^{-3} nm^3, respectively. Moreover, CTE of Ni_2Al_3 is reported to be 13 x 10^{-6} / ºC. When the initial diameter and core diameter are given, the total diameter after reaction, as well as the thickness of interlayer can be

estimated, and results are listed in Table 4. It should be noted that the diameter of core region becomes smaller when the total diameter becomes larger. Moreover, almost same interlayer thickness was found for swaged specimens, which is in agreement with experimental data. Swaging process before heating may accelerate the reaction. During the swaging process, the oxidation layer on the Al fiber was broken. Moreover, defects in solid Ni induced by the swaging enhance the diffusion rate of the solid state. These two phenomena enhance the reactions.

Table 4 Estimated core diameters in swaged specimens.

Initial Fiber Diameter	Core Diameter	Estimated Total Diameter	Layer Thickness
944μm	886μm	966μm	40μm
833μm	790μm	851μm	30μm
722μm	683μm	738μm	27μm
611μm	563μm	628μm	32μm

3.3 Hardness

Predicted from the microstructures, the position dependence of the hardness along the radial direction was observed. This is because the micro-hardness value of Ni, Ni_3Al, NiAl, Ni_2Al_3, $NiAl_3$, as-cast Al phases and eutectic $NiAl_3$ + Al structure is reported to be 180HV (Horie et al., 1985), 300HV (Tsao and Yeh, 2015), 620HV (Horie et al., 1985), 800-900HV (Kim et al., 2005) or 1500HV (Garbala and Patejuk, 2010), 1300HV (Garbala and Patejuk, 2010), 15HV (Watanabe et al., 2018) and 40-60HV (Yaseen et al., 1983), respectively. The size of indentation was few tens micrometer. Figures 19 (a) to (f) show the micro-hardness distributions within the specimens 1 to 6, respectively. In this figure, the abscissa represents the position in the radial direction of the fibers, where 0 μm corresponds to the center of the fiber.

As seen from Figs. 19 (a) and (b), the specimens processed at 660 ºC and 800 ºC (specimens 1 and 2) have very low hardness at the fibers, since these specimens have ($NiAl_3$ + Al) eutectic structure with small amount of primary Al and $NiAl_3$ phases, respectively. The fiber region has a constant hardness of around 25HV and 50 HV for specimens 1 and 2, respectively. Moreover, it is concluded that hardness gradient cannot be introduced by the lower processing temperatures.

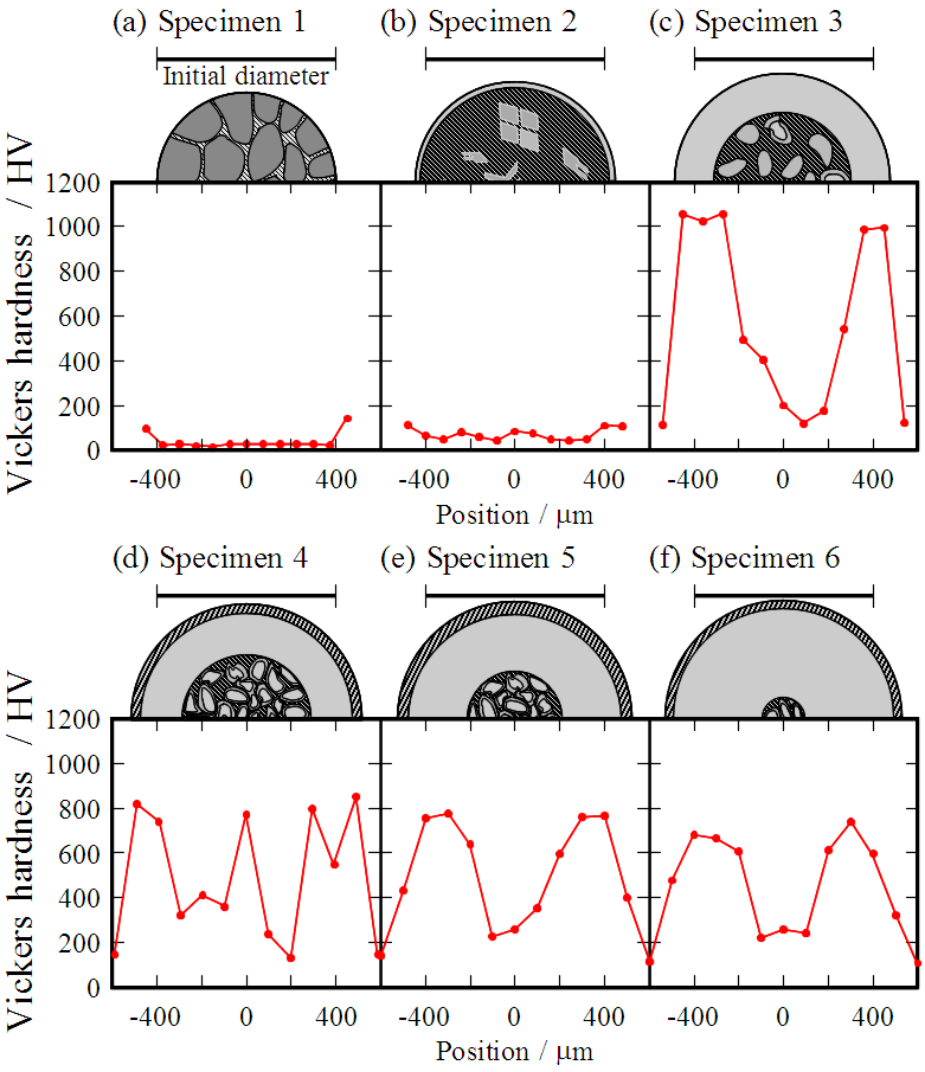

Fig. 19 Micro-hardness distributions within the specimens 1 to 6.

It must be noted that the specimen processed at 1000 ºC (specimen 3 shown in Fig. 19 (c)) has relatively low hardness at the center region of the fiber with ($NiAl_3$ + Al) eutectic structure, while as high as 1000-1100 HV at interface region with Ni_2Al_3 phase. In this way, the fabricated fiber in the specimen 3 has a stepwise hardness profile.

In case of the specimen 4 processed at 1200 ºC for 30 min (Fig. 19 (d)), the position dependence of the hardness along the radial direction is also found. Namely, this fiber has high hardness region at interface and scattered hardness region at core. This scattered hardness comes from relatively large size of intermetallic compounds, formed by crystallization or peritectic reaction, dispersed in the ($NiAl_3$ + Al) eutectic structure matrix.

The most remarkable result shown in Figs. 19 (e) and (f) is that the hardness is gradually distributed and the distributions show symmetry in the specimens 5 and 6, although stepwise hardness profile is found in the specimen processed at 1000 ºC (Specimen 3). HV values at core regions are higher than 200HV for both specimens 5 and 6. The graded hardness may provide good bonding between the intermetallic compound layer having a high hardness and the matrix metal having a low hardness, since the mechanical properties' gap becomes smaller. Lie et al. (2016) have investigated bonding characteristic in multi-layer laser cladding of NiCoCr alloy on graphite cast iron. In their study, they have reported that a gradual distribution of micro-hardness in the multi-layer clad coating layer reduces bonding brittleness. It is, therefore, expected that these specimens may provide higher mechanical properties, such as proof stress, tensile strength and bending strength, than specimens without graded microstructures. Detailed mechanical properties of nickel-aluminides fiber reinforced Ni matrix composites will be appeared in a future report.

Conclusions

In this study, Ni-aluminides long-fiber / Ni matrix composites are fabricated by the novel RANH method under various process conditions. Narrow hole is drilled in the Ni matrix, and then Al fiber is inserted into the hole. The assembly is heated to elevated temperatures (660 ^{o}C, 800 ^{o}C, 1000 ^{o}C and 1200 ^{o}C) to obtain molten Al in the hole. Then the reaction between Ni and A causes within the narrow hole. During the reaction, intermetallic compound of Ni-aluminides replaces the Al keeping its fiber shape embedded in the Ni matrix. The microstructure of the fiber in specimen changes depending on process conditions. This microstructural change can be explained based on Al-Ni phase diagram. Swaging process before heating accelerates the reaction. From these results, it is possible to control the microstructure of the fiber in specimen by process conditions. The hardness is gradually distributed in the specimens processed at higher temperature. It is also possible to control the hardness distribution in the specimen by process conditions.

ACKNOWLEDGEMENTS

This work was partly supported by The Light Metal Educational Foundation Inc. of Japan and Ministry of Education, Culture, Sports, Science and Technology (Regional Innovation Cluster Program, (Global Type). The authors are grateful to Ms. Motoko Yamada for her helpful work in carrying out the experiments.

References

Choi, Y.B., Matsugi, K., Sasaki, G., 2013. Development of intermetallic compounds reinforced Al alloy composites using reaction of porous nickel and aluminum, *Mater. Trans.* **54** (4), 595-598.

Ciuca, O., Tsuchiya, K., Yokoyama, Y., Todaka, Y., Umemoto, M., 2009. Effect of nanocrystallization and twinning on hardness in Ni3Al deformed by high-pressure torsion, *Mater. Trans.* **50** (5), 1123-1127.

Colgan, E.G., Nastasi, M., Mayer, J.W., 1985. Initial phase formation and dissociation in the thin‐film Ni/Al system, *J. Appl. Phys.* **58** (11), 4125-4129.

Darolia, R., 1991. NiAl alloys for high-temperature structural applications, *JOM* **43** (3), 44-49.

Garbala, K., Patejuk, A., 2010. Defects of Al-Ni joints caused by Kirkendall - Frenkel effect, *Arch. Found. Eng.* **10** (S1), 455-458.

Herrmann M., Schencka, C., Kuhfussa, B., 2016. Dry rotary swaging with structured tools, Procedia CIRP **40**, 653-658.

Honma, T., Terada, Y., Miura, S., Mohri, T., Suzuki, T., 1998. Gruneisen parameters in intermetallic compounds NiAl and Ni_3Al, Proceedings of the 1998 International Symposium on Advanced Energy Technology, 699-704.

Horie, Y., Graham, R.A., Simonsen, I. K., 1985. Synthesis of nickel aluminides under high-pressure shock loading, *Mater. Lett.* **3** (9-10), 354-359.

Janssen, M. M. P., Rieck, G. D., 1967. Reaction diffusion and Kirkendall-effect in the nickel-aluminum system, *Trans. Metal. Soc. AIME* **239**, 1372-1385.

Kim, H.-Y., Chung, D.-S., Hong, S.-H., 2005. Reaction synthesis and microstructures of NiAl/Ni micro-laminated composites, *Mater. Sci. Eng.* **A 396** (1-2), 376-384.

Lebrat, J.–P., Varma, A., Miller, A. E., 1992. Combustion synthesis of Ni_3Al and Ni_3Al-matrix composites, *Metal. Trans. A* **23A** (1), 69-76.

Leitner, M., Leitner, T., Schmon, A., Aziz, K., Pottlacher, G., 2017. Thermophysical properties of liquid aluminum, *Metall. Mater. Trans. A* **48** (6), 3036-3045.

Lieblich, M., Gonzarlez-Carrasco, J. L., Caruana, G., 1997. Thermal stability of an Al/Ni_3Al composite processed by powder metallurgy. *Intermetallics* **5** (7), 515- 524.

Liu, H., Hao, J. B., Han, Z. T., Yu, G., He, X. L., Yang, H. F., 2016. Microstructural evolution and bonding characteristic in multi-layer laser cladding of NiCoCr alloy on compacted graphite cast iron, *J. Mater. Process. Technol.* **232**, 153-164.

Ma, E., Thompson, C.V., Clevenger, L.A., 1991. Nucleation and growth during reactions in multilayer Al/Ni films: The early stage of Al_3Ni formation, *J. Appl. Phys*. **69** (4), 2211-2218.

Massalski, T. B., Editor-in-Chief, 1996. *Binary Alloy Phase Diagrams, Second Edition Plus Updates on CD-ROM* Version 1.0, ASM International, Ohio.

~~Miller, R. R., 1954. "Physical properties of liquid metals" in ``Liquid-metals Handbook, 2nd edition (revised), Chapter 2", R. N. Lyon (Editor-in-chief), U. S. Government Printing Office, Washington D. C., pp. 40.~~

Miura, S., Ohashi, T., Mishima, Y., 1997. Amount of liquid phase during reaction synthesis of nickel aluminides, *Intermetallics* **5** (1), 45-59.

Miura, S., Takizawa, S., Suzuki, T., Mishima, Y., Mohri, T., 2005. Effect of tetragonal distortion introduced by anti-site defect configuration on additional hardening in off-stoichiometric Al-rich Ni_3Al alloys, *Acta Mater*. **53** (19), 5175 – 5181.

Mizuuchi, K., Inoue, K., Sugioka, M., Itami, M., Lee, J.-H., Kawahara, M., 2006. Properties of Ni-aluminides-reinforced Ni-matrix laminates synthesized by pulsed-current hot pressing (PCHP), *Mater. Sci. Eng.* **A 428** (1-2), 169-174.

Morsi, K., 2001. Review: reaction synthesis processing of Ni–Al intermetallic materials, *Mater. Sci. Eng.* **A299** (1-2), 1-15.

Suzuki, T., Mishima, Y., Miura, S., 1989. Plastic behaviour in Ni_3 (Al, X) single crystal –Temperature, strain-rate, orientation and composition–, *ISIJ Int.* **29** (1), 1-23.

Tsao, C.-L., Chen, S.-W., 1995. Interfacial reactions in the liquid diffusion couples of Mg/Ni, Al/Ni and Al/(Ni)-Al_2O_3 systems, *J. Mater. Sci.* **30** (20), 5215-5222.

Tsao, T.-K., Yeh, A.-C., 2015. The thermal stability and strength of highly alloyed Ni_3Al, *Mater. Trans.* **56** (11), 1905-1910.

Venkatesh, T. A., Dunand , D. C., 1999. A model for the longitudinal primary creep of a long-fiber composite, *Acta Mater.* **47** (17), 4275-4282.

Watanabe, Y., Eryu, H., Matsuura, K., 2001a. Evaluation of three-dimensional orientation of Al_3Ti platelet in Al based FGMs fabricated by a centrifugal casting technique. *Acta Mater.* **49** (5), 775-783.

Watanabe, Y., Goto, T., 2003. Fabrication of nickel-aluminides fiber / nickel composite by reaction at narrow holes, *Mater. Sci. Forum* **426-432**, 1957-1962.

Watanabe, Y., Zhou, Q., Sato, H., Fujii, T., Inamura, T., 2017. Microstructure of Al-Al_3Ti functionally graded materials fabricated by centrifugal solid-particle method and centrifugal in situ method, *Jpn J. Appl. Phys.*, **56** (1S), 01AG01 (11 pages).

Watanabe, Y., Maekawa, K., Sato. H., 2018. Heterogeneous nucleation of α-Al primary crystal on $L1_2$ modified $Al_{2.7}Ni_{0.3}Ti$ phase, *Jpn J. Appl. Phys.*, **57** (1S), 01AF08 (6 pages).

Yaseen, R. S., Dwarakadasa, E. S., Ismail, A. R. 1983. Subsurface damage during dry sliding wear of Al-Al_3Ni eutectic alloy, *Wear* **85** (2), 213-221.

Figure captions

Fig. 1 Fabrication process of long fiber / metal matrix composite by RANH method.

Fig. 2 Ni-Al phase diagram (Massalski, 1996).

Fig. 3 The heat pattern and DTA profile.

Fig. 4 Result of *in-situ* observation by laser scanning microscope. The Al fiber at the center of the specimen was melted at around its melting temperature.

Fig. 5 and Fig. 6 Cross section view of the specimen 1 and specimen 2, respectively. Lower magnification photographs are shown in (a), whereas higher magnification photographs at fiber center region and the fiber / matrix interface region are shown in (b) and (c), respectively.

Fig. 7 Cross section view of the specimen 3. Lower magnification photographs are shown in (a), whereas higher magnification photographs at fiber center region and the fiber / matrix interface region are shown in (b) and (c), respectively.

Fig. 8 Schematic illustrations showing the final microstructure of specimens 1 to 3.

Fig. 9 Expected microstructural evolution of specimens 4 to 6 processed at 1200 ^{o}C. Initial state and microstructural evolution at 1200 ^{o}C are shown in (a) and (b), respectively. Shrinkage of core region and expansion of interlayer must be appeared by the time evolution, as shown in (c). Microstructural evolution during the cooling from 1200 ^{o}C to 1133 ^{o}C is shown in (d). (e) and (f) show the reaction around the interface region and final microstructures of specimens 4 to 6, respectively.

Fig. 10 Cross section view of the specimen 4. Lower magnification photographs are shown in (a), whereas higher magnification photographs at the fiber / matrix interface region are shown in (b).

Fig. 11 Cross section view of the specimen 5. Lower magnification photograph and higher magnification photograph at the fiber / matrix interface region are shown in (a) and (b), respectively. Concentration profiles of Al and Ni across the interlayer region are shown in (c).

Fig. 12 Cross section view of the specimen 6. Lower magnification photographs are shown in (a), whereas higher magnification photographs at fiber center region and the fiber / matrix interface region are shown in (b) and (c), respectively. Results of EDX analysis is shown in (d).

Fig. 13 Schematic illustrations of fiber before and after the reaction.

Fig. 14 Composition dependence of average atomic volume in Al-Ni binary system after Miura et al. (2005).

Fig. 15 Relation between d_1 and d_2 at 1200 ^{o}C. Calculation was carried out for n_1 = 0.72 and n_2 = 0.58, n_1 = 0.72 and n_2 = 0.50, and n_1 = 0.80 and n_2 = 0.50.

Fig. 16 Experimentally obtained relation between d_1 and d_2.

Figs. 17 (a), (b), (c) and (d) Cross section views of the specimens 7, 8, 9 and 10.

Fig. 18 SEM SEI images showing core region (a) and fiber / Ni matrix interface (b) in Specimen 7.

Fig. 19 Micro-hardness distributions within the specimens 1 to 6.